RSC Advances

PAPER

View Article Online
View Journal | View Issue

Cite this: *RSC Adv.*, 2023, **13**, 20951

The synthesis and super capacitive characterization of microwave-assisted highly crystalline α-Fe_2O_3/Fe_3O_4 nanoheterostructures†

Rajendra Panmand,[a] Yogesh Sethi,[a] Animesh Jha[b] and Bharat Kale*[a]

Received 25th March 2023
Accepted 23rd June 2023

DOI: 10.1039/d3ra01967e

rsc.li/rsc-advances

A facile microwave-assisted solvothermal process for the synthesis of narrow-size distributed α-Fe_2O_3, α-Fe_2O_3/Fe_3O_4, and Fe_3O_4 nanostructures was demonstrated using PVP as a surfactant. During the reaction, the influence of the reaction media, such as the mixture of ethylene glycol and water on the formation of α-Fe_2O_3, α-Fe_2O_3/Fe_3O_4, and Fe_3O_4 was systematically studied. Interestingly, pure aqueous medicated solvothermal reaction conferred phase pure rhombohedral Fe_2O_3 (hematite) and linearly upsurging the formation of cubic Fe_3O_4 (magnetite) with the increasing concentration of EG and further, in pure EG, it deliberated cubic Fe_3O_4. FESEM and FETEM images of α-Fe_2O_3/Fe_3O_4 nano heterostructure clearly showed the nanosized Fe_3O_4 particles of 4–6 nm decorated onto Fe_2O_3 nanoparticles. Further, the electrochemical properties of α-Fe_2O_3, α-Fe_2O_3/Fe_3O_4, and Fe_3O_4 nanoparticles were investigated with galvanostatic charge–discharge and cyclic voltammetry measurements using a 3-electrode system. The findings show that their specific capacitances are linked to the type of iron oxide. More significantly, the α-Fe_2O_3/Fe_3O_4 nanoheterostructure exhibited the utmost capacitance of 165 F g^{-1}, which is greater than that of pristine α-Fe_2O_3 and Fe_3O_4. Enhancement in the electrochemical performance was found due to the improved charge transfer that occurred at the interface of the nanoheterostructure. The nanoparticles of Fe_3O_4 deposited on the Fe_2O_3 increased the active sites, which accelerated the process of adsorption and desorption of ions, thereby enhancing the interface-assisted charge transfer and reducing the internal resistance, which is ultimately responsible for enhanced capacitance. Such heterostructures of nano iron oxide may fulfill the requirements of electrodes in supercapacitors.

Introduction

The engineering of supercapacitors for electrical charge storage is an emerging technology where the materials used must demonstrate higher power (*P*) and energy density, much-enhanced reversibility, and longer cycle life when compared with batteries and common capacitors.[1–4] The electrochemical capacitor was categorized as electric double-layer capacitors (ELDCs) or Faraday pseudocapacitors depending on the energy storage mechanism.[5–8] As compared to EDLCs, faradaic pseudocapacitors exhibit greater energy density (*E*) and specific capacitance owing to their reversible multi-electron redox/faradaic reactions.[9]

In general, transition metal oxides (TMOs) are used as electrode materials for pseudocapacitors. TMOs are promising materials as electrodes in pseudo or redox supercapacitors because of the increased *E* as a result of redox reactions. Amongst the TMOs, ruthenium dioxide (RuO_2) is recognized as the most promising electrode material owing to its good electrical conductivity and multiple redox states.[10] However, owing to its high cost and toxicity, RuO_2 is limited in its practical applications, thus other metal oxides that are inexpensive and environmentally friendly have gained significance in the areas of supercapacitors. In this respect, transition metal oxides, such as MnO_2,[11] NiO,[12] Co_2O_3,[13] Cu_xO,[14] V_2O_5,[15] SnO_2,[16a] and a few binary metal oxides, such as $NiMoO_4$,[16b,c] have been identified as potential alternatives to RuO_2. Recently, hematite (Fe_2O_3) and magnetite (Fe_3O_4) have emerged as promising oxide materials for supercapacitors, as both oxide forms are abundant in nature and non-toxic.[17a,b] Iron oxides (Fe_3O_4 and Fe_2O_3) are predicted for use as electrode materials with negative potential windows, large theoretical capacitance, and unique reversible redox reactions (Fe^{2+}/Fe^{3+}).[18] However, the '*P*', supercapacitance and corresponding small '*E*' of the Fe_2O_3 electrode are still quite low due to its very low electrical conductivity ($\sim 10^{-14}$ S cm^{-1}).[19] Significant research has been carried out to overcome the limitations. Notably, a number of approaches, such as the synthesis of doped Fe_2O_3 electrodes, nanostructured Fe_2O_3 electrodes, core–shell nanorod arrays, oxygen vacancy-induced

---

[a] Nanocrystalline Materials Division Centre for Materials for Electronics Technology (CMET), Panchawati, Off Pashan Road, Pune 411007, India. E-mail: rpanmand@gmail.com

[b] School of Chemical and Process Engineering, University of Leeds, Leeds LS2 9JT, UK

† Electronic supplementary information (ESI) available. See DOI: https://doi.org/10.1039/d3ra01967e

Fe_2O_3 electrodes, and Fe_2O_3 composite electrodes have been investigated.[20–23] Amongst these approaches, the fabrication of Fe_2O_3 composite electrodes with graphene,[24] mesoporous carbon,[25] PANI,[26] and SnO_2 (ref. 27) was also investigated. Although the enhanced super capacitive performance was attained, the limited electronic and ion transport remains a critical concern for Fe_2O_3 composites to be high-performance electrodes. Very few reports are available on the synthesis of the composite of Fe_2O_3 and highly conductive Fe_3O_4 for energy storage applications. Tang *et al.* reported enhanced electrochemical performance due to the improvement in the charge transport of Fe_3O_4/Fe_2O_3 composites.[21]

Synthesis of Fe_3O_4 nanoparticles using monovalent precursor is quite difficult and hence many reports on Fe_3O_4 preparation involve mixing Fe^{2+} and Fe^{3+} in different ratios.[28] Herein, we have synthesized the nanostructured Fe_2O_3, Fe_3O_4/Fe_2O_3 nanoscale heterostructure, and Fe_3O_4 using monovalent precursor ($FeCl_3 \cdot 6H_2O$) using the facile microwave method. The formation of nanoscale heterostructure was demonstrated by a microwave solvothermal method using water ethylene glycol mixture as a reaction medium. The details of the electrochemical characterization of the nanoscale heterostructure materials are also discussed alongside the capacitance measurements. The influence of nano-scale phase combination on capacitance is compared and discussed in terms of charge storage.

Experimental

All chemicals used here, namely ferric chloride ($FeCl_3$, >99.9%), sodium hydroxide (NaOH, >99.0%), ethylene glycol (EG, >99.0%), were procured from SD Fine Chemicals Ltd, Mumbai, India and no further purification step was adopted for the synthesis of nanoparticles of iron oxides.

For the synthesis of nanoparticles of iron oxide, 0.35 g (50 mM) $FeCl_3 \cdot 6H_2O$, 0.3 g (150 mM) NaOH were mixed with 20 mL of ethylene glycol and water in a 100 mL beaker, as shown in Table 1. The homogenous solution was sealed in a double-walled digestion vessel lined with Teflon. A Milestone's Start D microwave digestion system oven equipped with a solution digester stage was used for heating the solutions containing $FeCl_3$/NaOH with EG for 25 min to a controlled temperature of 150 °C. After the microwave digestion, each solution, listed in Table 1, was cooled to room temp. After centrifugal separation, the product was taken and washed in deionized water and 100% ethanol. For four hours, the reaction product was dried at 80 °C in a vacuum.

Table 1 Water to ethylene glycol ratio used in reactions

Sample ID	Solvent	Volume ratio
F1	Water	—
F2	Water : EG	3 : 1
F3	Water : EG	2 : 2
F4	Water : EG	1 : 3
F5	EG	—

The phase purity, structural, and morphological and microstructural analyses of the synthesized iron oxide phase mixtures including heterostructure were examined using an X-ray Powder Diffractometer XRD (Bruker (D8)), HR 800-Raman Spectroscopy (Horiba Joblin Yvon, France), and FESEM (FEI NOVANANOSEM 450), respectively.

Electrochemical measurements

Carbon paper was used for making electrodes for electrochemical testing. For each measurement, two carbon paper electrodes with similar surface areas were utilized. The Fe_2O_3/Fe_3O_4 nanoparticles were loaded onto the carbon paper as a substrate, as shown below. Thus, 80 wt% Fe_2O_3/Fe_3O_4 was added to 10 wt% polyvinylidene fluoride (PVDF) and acetylene black each. The viscous slurry was prepared by adding 5–7 mL of NMP (*N*-methyl-2-pyrrolidone) into the above mixture. The carbon paper substrate was then covered with this slurry. The electrodes were dried for 6–7 hours at 100 °C. In an aqueous 6 M KOH solution, electrochemical cyclic voltammetry experiments were performed from the −1 to 0.2 V range of potential at varied scan rates.

Electrochemical impedance spectroscopy study

Electrochemical impedance (EI) spectroscopy measurements were executed for a symmetrical supercapacitor cell made up of Fe_2O_3/Fe_3O_4 nanoparticles in an aqueous 1 M Na_2SO_4 electrolyte. The study was performed using a frequency of 10 kHz to 10 MHz range and AC amplitude of 10 mV without the use of an external DC applied voltage.

Results and discussion

The XRD patterns of the self-assembled bipyramidal-like α-Fe_2O_3/Fe_3O_4 nanoparticles are shown in Fig. 1a and b, prepared using different water-to-EG ratios as solvents. The XRD pattern of the pure aqueous mediated (F1) sample showed the presence of rhombohedral hematite without any impurity peaks (JCPDS no. 072-0469). Based on the powder diffraction data presented in Fig. 1a, the lattice constants were calculated for each sample, and it was determined that the values of lattice constants are $a = b = 5.030$ Å, $c = 13.87$ Å, which are comparable to the JCPDS

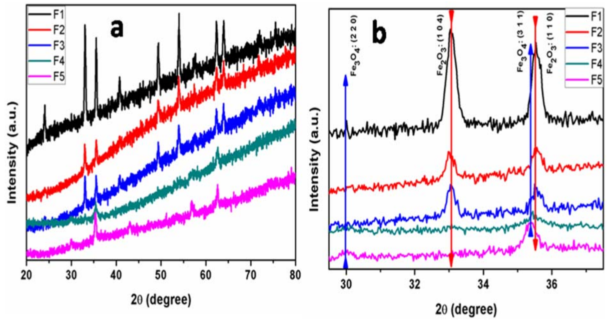

Fig. 1 Full XRD patterns (a) and magnified XRD pattern (b) of the α-Fe_2O_3/Fe_3O_4 prepared using different water to EG ratios as a solvent.

data for hematite powder ($a = b = 5.034$ Å and $c = 13.57$ Å). As the amount of the EG in the solvent increased to 50% (F3) and 75% (F4), the additional peaks of cubic magnetite (JCPDS-072-0748) (Fe_3O_4) and (Fe_2O_3-JCPDS no. 072-0469) appeared. The sample prepared using pure EG solvent (F5) showed the formation of cubic magnetite (JCPDS-074-0748). The magnified pattern (29.5 to 37.5°) is shown in Fig. 1b for clarity. From Fig. 1b, it is revealed that the XRD peak intensity of α-Fe_2O_3 (1 1 0) and (1 0 4) diminished with an increase in EG and other planes corresponding to Fe_3O_4 (2 2 0) and (3 1 1) appeared, distinctly. The Fe_2O_3, Fe_3O_4@Fe_2O_3 heterostructure and Fe_3O_4 can be easily prepared using Fe(III)Cl_3 and by varying the water to EG solvent ratio during the reaction.

The morphological evolution of the α-Fe_2O_3/Fe_3O_4 prepared at different water : EG ratios was conducted using FESEM. Fig. 2 shows the FESEM images at different magnifications of samples obtained with different EG : water ratios (F1, F3, and F5). Uniformity and homogeneity of particles can be revealed from low magnification FESEM images. However, high-magnification images are valuable for studying the effect of the solvent ratio on morphology. Fig. 1a and b show the FESEM images of sample F1 (made purely in water medium), which revealed the uniform and monodisperse self-assembled bipyramidal α-Fe_2O_3 nanoparticles of size 140–150 nm in length and 100–120 nm in diameter (see Fig. 1b). The bipyramidal α-Fe_2O_3/Fe_3O_4 nano-heterostructure nanoparticles with sizes 80–90 nm in length and 50–70 nm in diameter were observed for samples prepared using 1 : 1 EG to water ratio (F3 see Fig. 1d). However, when the sample was prepared using pure EG as the solvent (F5), monodispersed and spherical Fe_3O_4 nanoparticles of diameter 30–50 nm were formed without any other phase. From FESEM, it can be concluded that the nanoparticle size of the material declined with increasing EG concentration in the reaction medium. It is obvious because of the low dielectric constant of EG (37) compared to that of water (80), the ionic mobility slowed down, which ultimately controlled the formation and growth of the nanoparticle. Hence, the lower particle size obtained in pure EG is quite justifiable. Fig. 1g and h demonstrate the images of the samples F1 and F5 dispersed in water with and without an external magnetic field. From the image, it is clear that Fe_3O_4 nanoparticles (sample F5) are well dispersed in water before magnetic separation. However, all Fe_3O_4 NPs are attracted toward the magnet, after magnetic field application. For comparison, the α-Fe_2O_3 nanoparticles were also dispersed in water, however, there was no change before and after magnetic separation.

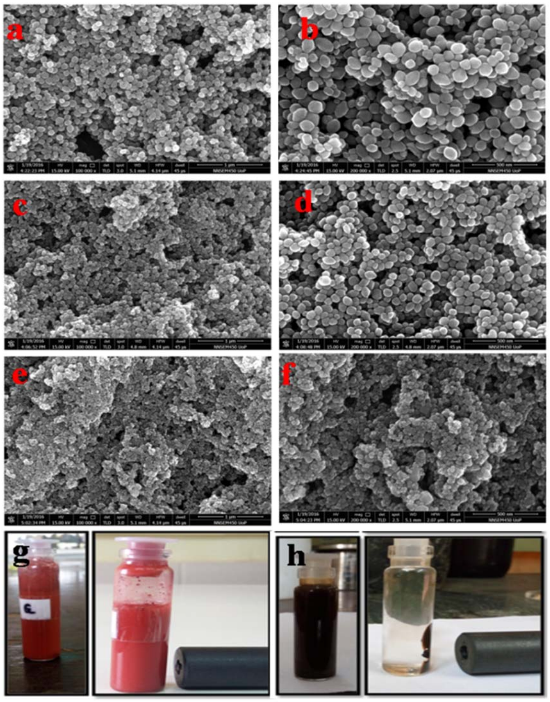

Fig. 2 Images of FESEM at low and high magnification of samples prepared at different EG : water solvent ratios. (a and b): F1, (c and d): F3 and (e and f): F5. Photographs of α-Fe_2O_3 NPs (g) and Fe_3O_4 NPs (h) before and after magnetic separation with an external magnetic field.

Being a magnetic sample, the sample was dispersed in PVA, and the film was employed for FETEM. Fig. 3 shows the TEM images of the Fe_2O_3/Fe_3O_4 nano-heterostructure prepared using a 1 : 3 water-to-EG solvent ratio. From TEM images, it is concluded that the tiny Fe_3O_4 nanoparticles of size 4–6 nm were grown on the Fe_2O_3 nanoparticles (see Fig. SI 1 in ESI†). TEM images clearly show that the entire Fe_2O_3 nanoparticles are covered with tiny Fe_3O_4. Fig. SF 2 from ESI† shows lattice-resolved HRTEM of Fe_2O_3-on-Fe_2O_3 nanoparticles. The interplanar spacing was measured to be about 0.367 nm, which is in good agreement with that of the (012) crystal plane. The SEAD pattern is poor due to the polymer film, which is given in the ESI.†

Raman spectra of iron oxide samples prepared using pure water (F1), water : EG in a 1 : 1 ratio (F3), and pure EG as the solvent (F5) are shown in Fig. 4. "The Raman spectra of the above-made F1 sample (α-Fe_2O_3 nanoparticles) do not contain the peaks belonging to Fe_3O_4. The peaks at 221 and 497 cm^{-1} are classified as A_{1g} modes, whereas the peaks at 244, 292, 406, and 611 cm^{-1} are classified as Eg modes".[29,30] From Raman spectra, the peaks in the spectrum of sample F5 (Fe_3O_4) at "305 and 534 cm^{-1} are reliably allocated to the T_{2g} mode, whereas the peak at 513 cm^{-1} is allocated to the Eg mode and the peak at 660 cm^{-1} is allocated to the A_{1g} mode". However, in sample F3, both iron oxide phase peaks were found, which confirmed the existence of nano-heterostructure.

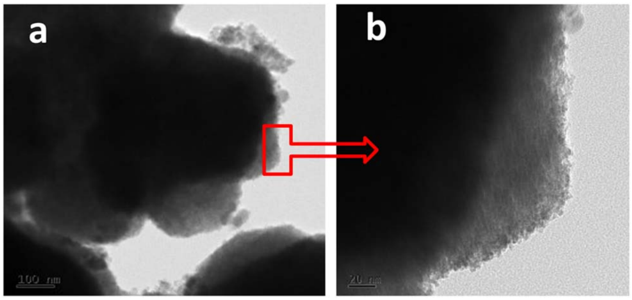

Fig. 3 TEM image of Fe_2O_3/Fe_3O_4 nanocomposite prepared at 1 : 3 water to EG solvent ratio.

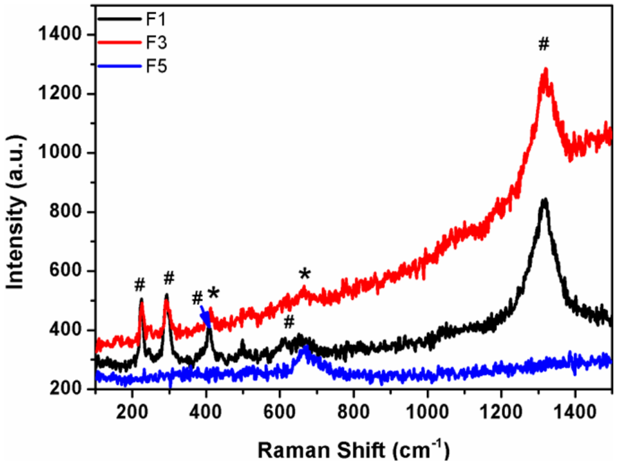

Fig. 4 Raman spectra of samples prepared at different EG : water solvent ratios.

Growth mechanism

Generally, the growth mechanism consists of two stages, *i.e.* nucleation of amorphous primary particles followed by slow crystallization and aggregation of primary particles.[31,32] In the present case, the diluted Fe^{3+} ion aqueous solution was directly digested under microwave hydrothermal conditions at 150 °C. The formation of α-Fe_2O_3 involved two stapes.[33,34a] Initially, It may be that β-FeOOH is formed by hydrolysis of $([Fe(H_2O)_6]^{3+})$ in an aqueous solution and further, the β-FeOOH undergoes a transformation to α-Fe_2O_3 *via* the dissolution/re-precipitation mechanism.[34b] EG is acting as a reducing agent apart from the solvent medium. Initially, it combined with $FeCl_3$ to form iron alkoxide nuclei, which then further grew at hydrothermal conditions and formed Fe_3O_4 nanoparticles of size 30–50 nm in size. However, in a mixture of EG and water solvent, the α-Fe_2O_3@Fe_3O_4 heterostructure was formed. The possible formation and growth mechanism are shown in Fig. 5. In aqueous EG, iron alkoxide formation along with FeOOH is quite understood. Preferentially, the formation of Fe_2O_3 from FeOOH takes place first, and then alkoxide gets reduced to Fe_3O_4. Hence, we can see the deposition of Fe_3O_4 nanoparticles on the Fe_2O_3 particle (Fig. 5). During the reaction, the average dielectric constant was decreased due to EG in the water, which ultimately controlled the growth of α-Fe_2O_3@Fe_3O_4 resulting in a lower nanoparticle size of α-Fe_2O_3/Fe_3O.

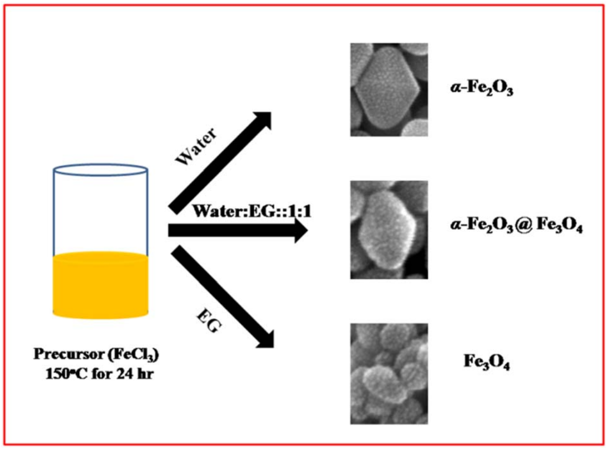

Fig. 5 The schematic representation of the growth mechanism.

Electrochemical study

Cyclic voltammetry (CV) is used to characterize the supercapacitive behavior of any material. The C_{sp} of the cell was evaluated from the CV curve as per the following equation:

$$C_{sp} = \frac{I}{\frac{dv}{dt}m} \tag{1}$$

Here, C_{sp} indicates the specific capacitance of a single electrode (in F g^{-1}), I indicate the discharge current (in A); m indicates the active materials mass (in g); dv/dt indicates the slope of the discharge curve. Fig. 6a–c illustrates the CV curves obtained for samples F-1, F-3, and F-5 electrodes using a 3-electrode cell system. The voltage scan rate was 5 to 100 mV s^{-1} in 6 M KOH electrolyte with the Pt plate as the counter electrode and an SCE ("saturated calomel electrode") as the reference electrode having a potential of −1.0–0.2 V range. Each sample's CV curve is approximately symmetrical, with small redox peaks. The cathodic peaks shift "negatively" while the anodic peaks shift "positively" with the increase in scan rates. The samples exhibit pseudocapacitive characteristics. When scan rates increased from 5 to 100 mV s^{-1}, the peak I increased with a negligible change in the CV shape, indicating its good electrochemical reversibility and high-power features. The CV curves have an obvious pair of redox peaks at −0.54 and −0.86 V. The presence of obvious redox peaks indicates good electrochemical performance attributed to the change in the Fe valence state, *i.e.*, F(II) ↔ Fe(III).[35a]

The galvanostatic charge–discharge curves and performance rate of the F-1, F-3, and F-5 samples with current densities ranging from 0.5 to 4 A g^{-1} are displayed in Fig. 6d–f. The modest charge–discharge platforms that are formed in samples F-1, F-3, and F-5, as shown in Fig. 6d–f, suggesting that tiny

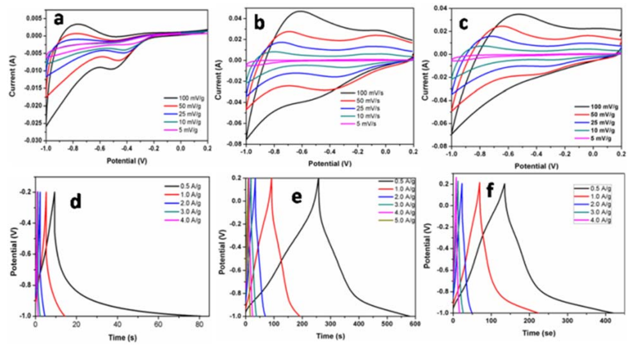

Fig. 6 Cyclic voltammeter (potential (V) *vs.* saturated calomel electrode) and galvanostatic charge–discharge curve of F1 (a and d), F3 (b and e), and F5 (c and f).

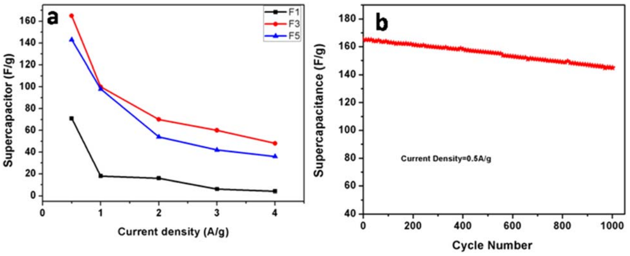

Fig. 7 (a) Specific capacitance calculated for F1, F3, and F5 based on the charge/discharge curves as a function of current densities. (b) Cycling stability of the F3 electrode collected at a current density of 0.5 A g^{-1} for 1000 cycles.

redox processes take place during the charge–discharge process. It is consistent with the modest redox peaks seen in the CV profile. In all three samples, there are 2 variance ranges that are present during the charge and discharge processes. The potential time dependence is linear and nonlinear below −0.4 V and above −0.4 V resp. in which the linear shows pure double-layer capacitance behaviour resulting from charge separation at the electrode–electrolyte interface[35b] while the nonlinear is due to the typical pseudo-capacitance behaviour. High specific capacitance values are produced at small current densities by completely accumulating charges in the electrode's inner active sites. The specific capacitances of F-1, F-2, and F-3 are 49, 165 and 157 F g^{-1} at 0.5 A g^{-1}, respectively. Due to the movement of electric charges being out of phase with current rates, the specific capacitance value declines as current density increases. At very fast charge–discharge, only the outer active surface of the electrode material is used for charge storage.[36] The specific capacitance change with current density is summarized in Fig. 7a and Table 2. As shown in Fig. 7a, the charge/discharge curves of the 3 electrodes collected at a 0.5 A g^{-1} current density showed that the sample F3 (Fe_3O_4@Fe_2O_3) electrode presented the most prolonged charge/discharge curves, confirming its outstanding capacitive performance than F1 (Fe_2O_3) and F5 (Fe_3O_4). Additionally, the internal resistance (IR) drop of 0.17 V for the F3 electrode was much smaller than 0.21 V for the F5 electrode, indicating the enhanced electrical conductivity of the F3 (Fe_3O_4@Fe_2O_3) electrode.

Fig. SI 3† shows the N_2 adsorption–desorption isotherms of the as-prepared F1, F2 and F3 heterostructures. The Brunauer–Emmett–Teller (BET) specific surface areas of F1, F2, and F3 heterostructures were measured to be 19.9, 34.5, and 32.14 m^2 g^{-1}, respectively. Results showed that the surface area of Fe_3O_4@Fe_2O_3 is higher than Fe_3O_4 and Fe_2O_3. Also, it has been reported that the junction formation at the Fe_2O_3/Fe_3O_4 interface can significantly improve the charge transport of Fe_3O_4@Fe_2O_3 composites.[37] Hence, Due to high surface area and improved charge transport, the Fe_3O_4@Fe_2O_3 shows improved capacitance than Fe_3O_4 and Fe_2O_3.

The cycling stability of the electrode materials used in supercapacitor applications is an additional essential parameter. "Constant current charge–discharge cycling" at a 0.5 A g^{-1} current density was recorded in order to assess the cycling stability of F3 electrodes (Fig. 7b). The calculated specific capacitance values were plotted as a function of cycle numbers (in Fig. 7b). A slight reduction of around 12% of the initial capacitance was found for the F3 electrode after 1000 cycles. The comparison of the present supercapacitor with the reported supercapacitor is shown in Table SI 1.† The table shows that our supercapacitor is superior to the reported values.

For energy storage devices, it is very important to know the value of '*E*' and '*P*'. The '*E*' and '*P*' are evaluated from the following equations:

$$E = \frac{1}{2} C_{sp} (\Delta V)^2 \tag{2}$$

$$P = \frac{E}{t_{dis}} \tag{3}$$

Here, C_{sp} indicates the specific capacitance of the active material, *t* indicates the discharging time and ΔV indicates the potential window in 6 M KOH for charging and discharging. Different current energies and '*P*' and specific capacitance for samples are presented in Table 2.

The relationship between '*E*' and '*P*', *i.e.*, the Ragone plot for F1, F3, and F5 is illustrated in Fig. 8. According to Fig. 8, F3 obtained an '*E*' of 33 W h kg^{-1} at '*P*' of 364.20 W kg^{-1} and retained 9.60 W h kg^{-1} at 2723.40 W kg^{-1}, both of which are greater than that of recently published Fe_2O_3/Fe_3O_4 symmetric supercapacitors in aqueous electrolyte.[38] The '*E*' observed for sample F3 at a current density 0.5 A g^{-1} is much higher than F1 and F5. The enhancement in the electrochemical properties in Fe_2O_3/Fe_3O_4 sample (F3) may be due to lower internal resistance and better charge transport, which arises from the junction produced at the Fe_3O_4/Fe_2O_3 interface than Fe_2O_3 (F1) and Fe_3O_4 (F5). These findings reveal that the synthesized F3 may

Table 2 The Specific capacitance change with current density

	F1			F2			F3		
Current density (A g^{-1})	C_s (F g^{-1})	*E* (W h kg^{-1})	*P* (W kg^{-1})	C_s (F g^{-1})	*E* (W h kg^{-1})	*P* (W kg^{-1})	C_s (F g^{-1})	*E* (W h kg^{-1}	*P* (W kg^{-1})
0.5	71	14.2	716	165	33	364.2	143	28.6	358.8
1	18	3.6	1440	100	20	711.6	98	19.6	456.5
2	16	3.2	3600	70	14	1374.8	54	10.8	1160.6
3	6	1.2	4320	60	12	2168.67	42	8.4	2131.1
4	4	0.8	5760	48	9.6	2723.4	36	7.2	3014.0

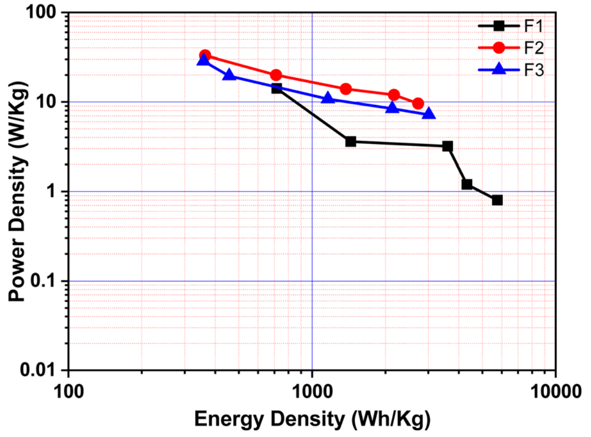

Fig. 8 Ragone plots for F1, F3, and F5 (plot of energy density *vs.* power density).

provide an excellent electrode material for supercapacitors with high power and low cost.

Conclusions

Herein, a facile microwave-assisted solvothermal route for the synthesis of Fe_3O_4/Fe_2O_3, Fe_2O_3, and Fe_3O_4 nanoparticles having narrow size distribution with $FeCl_3$ as the iron source was investigated. The phase of the iron oxide was tuned by varying the EG to water ratio in the solvent. The prepared Fe_3O_4/Fe_2O_3, Fe_2O_3, and Fe_3O_4 nanoparticles were studied for electrochemical application. The as-prepared Fe_3O_4/Fe_2O_3 heterostructures demonstrated greater specific capacitances of 165 F g^{-1} at the current density of 0.5 A g^{-1} than Fe_2O_3 and Fe_3O_4. In a nutshell, the findings of this study indicate that hematite might be used as an electrode material for high-performance supercapacitors.

Conflicts of interest

There are no conflicts to declare.

Acknowledgements

The authors would like to thank the Ministry of Electronics and Information Technology (MeitY), the Government of India's financial support for research, and C-MET Pune for providing research facilities. The authors would like to thank the Nanocrystalline Materials group, C-MET, Pune, and Microwave Materials Division, C-MET, Thrissur.

Notes and references

1 C. Hong, Y. Deng, W. Hu, J. Qiao, L. Zhang and J. Zhang, *Chem. Soc. Rev.*, 2015, **44**, 7484–7539.
2 D. P. Dubal, O. Ayyad, V. Ruiz and P. Gomez-Romero, *Chem. Soc. Rev.*, 2015, **44**, 1777–1790.
3 D. Chen, Q. Wang, R. Wang and G. Shenb, *J. Mater. Chem. A*, 2015, **3**, 10158–10173.
4 S. Faraji and F. Nasir Ani, *Renewable Sustainable Energy Rev.*, 2015, **42**, 823–834.
5 Y. Lu, K. Fu, S. Zhang, Y. Li, C. Chen, J. Zhu, M. Yanilmaz, M. Dirican and X. Zhang, *J. Power Sources*, 2015, **273**, 502–510.
6 D. Wang, Z. Geng, B. Li and C. Zhang, *Electrochim. Acta*, 2015, **173**, 377–384.
7 J. Liu, J. Jiang, C. Cheng, H. Li, J. Zhang, H. Gong and H. J. Fan, *Adv. Mater.*, 2011, **23**, 2076–2081.
8 Y. Zhang, H. Feng, X. Wu, L. Wang, A. Zhang, T. Xia, H. Dong, X. Li and L. Zhang, *Int. J. Hydrogen Energy*, 2009, **34**, 4889–4899.
9 L. Wang, H. Ji, S. Wang, L. Kong, X. Jiang and G. Yang, *Nanoscale*, 2013, **5**, 3793–3799.
10 M. Zhu, Y. Wang, D. Meng, X. Qin and G. Diao, *J. Phys. Chem. C*, 2012, **116**, 16276–16285.
11 J. Zhi, S. Deng, Y. Wang and A. Hu, *J. Phys. Chem. C*, 2015, **119**, 8530–8536.
12 V. Kannan, A. I. Inamdar, S. M. Pawar, H.-S. Kim, H.-C. Park, H. Kim, H. Im and Y. S. Chae, *ACS Appl. Mater. Interfaces*, 2016, **8**(27), 17220–17225.
13 T.-Y. Wei, C.-H. Chen, K.-H. Chang, S.-Y. Lu and C.-C. Hu, *Chem. Mater.*, 2009, **21**, 3228–3233.
14 A. Lamberti, M. Fontana, S. Bianco and E. Tresso, *Int. J. Hydrog. Gener.*, 2016, **41**, 11700–11708.
15 B. Saravanakumar, K. K. Purushothaman and G. Muralidharan, *ACS Appl. Mater. Interfaces*, 2012, **4**, 4484–4490.
16 (*a*) F. Li, J. Song, H. Yang, S. Gan, Q. Zhang, D. Han, A. Ivaska and L. Niu, *Nanotechnology*, 2009, **20**, 455602; (*b*) P. Sharma, M. M. Sundaram, T. Watcharatharapong, D. W. Laird, H. Euchner and R. Ahuja, *ACS Appl. Mater. Interfaces*, 2020, **12**(40), 44815–44829; (*c*) M. Minakshi and K. Wickramaarachchi, *Prog. Solid State Chem.*, 2023, **69**, 100390.
17 (*a*) P. A. Lu, M. R. Manikandan, P. F. Yang, Y. L. He, F. Yang, S. T. Dang, Y. C. Shi, W. B. Lou, R. Liu, S. J. Wu, X. F. Li, Y. C. Hu, J. Shang, S. Q. Yin and X. W. Wang, *J. Mater. Sci.: Mater. Electron.*, 2023, **34**, 826; (*b*) P. M. Anjana, J. F. Joe Sherin, C. Vijayakumar, S. R. Sarath Kumar, M. R. Bindhu and R. B. Rakhi, *Mater. Sci. Eng., B*, 2023, **290**, 116313.
18 V. D. Nithya and N. Sabari Arul, *J. Mater. Chem. A*, 2016, **4**, 10767–10778.
19 Z. Song, W. Liu, W. Wei, C. Quan, N. Sun, Q. Zhou, G. Liu and X. Wen, *J. Alloys Compd.*, 2016, **685**, 355–363.
20 X. Du, C. Wang, M. Chen, Y. Jiao and J. Wang, *J. Phys. Chem. C*, 2009, **113**, 2643–2646.
21 X. Tang, R. Jia, T. Zhai and H. Xia, *ACS Appl. Mater. Interfaces*, 2015, **7**, 27518–27525.
22 K. Karthikeyan, S. Amaresh, S. N. Lee, V. Aravindan and Y. Sung Lee, *Chem.–Asian J.*, 2014, **9**, 852–857.
23 D. Sarkar, G. G. Khan, A. K. Singh and K. Mandal, *J. Phys. Chem. C*, 2013, **117**(30), 15523–15531.
24 M. Saraf, K. Natarajan and M. M. Shaikh, *RSC Adv.*, 2017, **7**, 309.
25 J. Hu, M. Noked, E. Gillette, F. Han, Z. Gui, C. Wang and S. Bok Lee, *J. Mater. Chem. A*, 2015, **3**, 21501–21510.

26 P. M. Padwal, S. L. Kadam, S. M. Mane and S. B. Kulkarni, *J. Mater. Sci.*, 2016, **51**, 10499.

27 R. Lei, H. Ni, R. Chen, B. Zhang, W. Zhan and L. Yang, *Chem. Phys. Lett.*, 2017, **673**, 1–6.

28 P. Panneerselvam, N. Morad and K. Aik Tan, *J. Hazard. Mater.*, 2011, **186**, 160–168.

29 A. G. Nasibulin, S. Rackauskas, H. Jiang, Y. Tian, P. Reddy Mudimela, S. D. Shandakov, L. I. Nasibulina, J. Sainio and E. I. Kauppinen, *Nano Res.*, 2009, **2**, 373–379.

30 C. Zhao, X. Shao, Y. Zhang and X. Qian, *ACS Appl. Mater. Interfaces*, 2016, **8**(44), 30133–30142.

31 L.-S. Zhong, J.-S. Hu, H.-P. Liang, A.-M. Cao, W.-G. Song and L.-J. Wan, *Adv. Mater.*, 2006, **18**, 2426–2431.

32 X. Hu, J. C. Yu, J. Gong, Q. Li and G. Li, *Adv. Mater.*, 2007, **19**, 2324–2329.

33 Z. Pu, M. Cao, J. Yang, K. Huang and C. Hu, *Nanotechnology*, 2006, **17**, 799–804.

34 (*a*) M. Lin, H. R. Tan, J. P. Ying Tan and S. Bai, *J. Phys. Chem. C*, 2013, **117**(21), 11242–11245; (*b*) C.-Y. Yin, M. Minakshi, D. E. Ralpha, Z.-T. Jiang, Z. Xie and H. Guo, *J. Alloys Compd.*, 2011, **509**, 9821–9825.

35 (*a*) R. Li, X. Ba, Y. Wang, W. Zuo, C. Wang, Y. Li and J. Liu, *Prog. Nat. Sci.: Mater. Int.*, 2016, **26**, 258–263; (*b*) J. Wang, L. Zhang, X. Liu, X. Zhang, Y. Tian, X. Liu, J. Zhao and Y. Li, *Sci. Rep.*, 2016, **7**, 41088.

36 R. P. Panmand, P. Patil, Y. Sethi, S. R. Kadam, M. V. Kulkarni, S. W. Gosavi, N. R. Munirathnam and B. B. Kale, *Nanoscale*, 2017, **9**, 4801–4809.

37 B. Lei, D. Xu, B. Wei, T. Xie, C. Xiao, W. Jin and L. Xu, *ACS Appl. Mater. Interfaces*, 2021, **13**, 4785–4795.

38 X. Tang, R. Jia, T. Zhai and H. Xia, *ACS Appl. Mater. Interfaces*, 2015, **7**(49), 27518–27525.